JOURNAL OF SPACECRAFT AND ROCKETS
Vol. 46, No. 5, September–October 2009

Pointing-Stability Performance of the Cassini Spacecraft

Emily B. Pilinski* and Allan Y. Lee†
Jet Propulsion Laboratory, California Institute of Technology, Pasadena, California 91109-8099

DOI: 10.2514/1.41675

The operations of Cassini optical remote sensing instruments require a high level of spacecraft-pointing stability to minimize image distortion during an exposure window. This paper summarizes the flight performance of the Cassini spacecraft's pointing stability with respect to mission requirements. Sources of spacecraft jitter, the Cassini spacecraft control modes, and pointing-stability metrics are discussed to provide a context for the results. In designing the Cassini attitude-control system, a pointing-stability performance metric that considered the frequency contents of the disturbance sources was employed. Cassini pointing-stability results using the root-mean-square stability metric are provided for both spacecraft control modes, using the reaction-wheel assembly or the reaction control system composed of eight thrusters. The pointing-stability results are then related to characteristics of the spacecraft and operations. For thruster-based control, the pointing-stability results are analyzed with respect to the per-axis dead band. Results from the scientific instruments onboard the Cassini spacecraft confirm that the pointing-stability results in either control mode have achieved high accuracy pointing capabilities critical to the success of the mission and have resulted in data to improve our understanding of Saturn.

Nomenclature

C	=	normalized frequency, dimensionless
e	=	deviation of line-of-sight vector from its windowed mean, rad
F	=	magnitude of thruster force, N
f	=	frequency of a time signal, Hz
I_{ZZ}	=	Z-axis moment of inertia of the spacecraft, kg · m^2
L	=	moment arm of the thrusters, m
m	=	windowed mean of the line-of-sight vector, rad
N	=	number of exposure windows in a telemetry sample, dimensionless
s_p	=	windowed peak stability, rad
T	=	exposure time of an imaging event, s
W	=	frequency weighting function, dimensionless
ΔT_{pulse}	=	duration of thruster pulse, s
$\Delta\theta$	=	rms pointing-stability performance defined in Eq. (10), rad
σ_{rms}	=	rms stability metric, rad
σ^2_{SP}	=	squared peak stability metric, rad^2
σ^2_W	=	windowed variance of the line-of-sight displacement vector, rad^2
Φ_{PSD}	=	power spectral density of the signal ϕ, rad^2/Hz
ϕ	=	time history of the angular displacement of the line-of-sight vector, rad
Ω	=	Z-axis spacecraft rate, rad/s

Presented as Paper 6810 at the AIAA Guidance, Navigation, and Control Conference and Exhibit, Honolulu, HI, 18–21 August 2008; received 17 October 2008; revision received 11 April 2009; accepted for publication 17 April 2009.

*Guidance and Control Systems Engineer; currently Mission Operations Lead, BioServe Space Technologies/University of Colorado, Boulder, Colorado 80309; Emily.Pilinski@colorado.edu.

†Project Element Manager, Attitude and Articulation Control System, Cassini Spacecraft Operations Office, Mail Stop 230-104, 4800 Oak Grove Drive; Allan.Y.Lee@jpl.nasa.gov.

I. Introduction

THE Cassini orbiter is a platform for extensive exploration of the Saturn system, including Saturn, its moons, and its rings. The spacecraft carries 12 scientific instruments on a seven-year, 1.5×10^9 km mission. The Cassini mission, the spacecraft, and the instruments are described in detail in [1]. The four-year prime mission concluded in July 2008 and is succeeded by a two-year extended mission. This paper will characterize Cassini's pointing stability from data collected during the prime tour operations during which the spacecraft was controlled by either the reaction-wheel assembly (RWA) or the reaction control system (RCS). Since Cassini's launch on 15 October 1997, spacecraft attitude has been routinely estimated onboard and telemetered to the operations engineering team. Using these data, this paper documents our effort to better characterize the pointing-stability performance of the Cassini spacecraft during the four-year prime mission. By studying the stability performance of Cassini in relation to the spacecraft design characteristics and operations, this work documents the practices that have resulted in precision jitter control to maximize science return.

The Spacecraft Operations Office (SCO) at the Jet Propulsion Laboratory focuses on protecting this scientific platform from the harsh space environment to ensure the reliability of the spacecraft's sensors and equipment on which the science return depends. A group within SCO, the Attitude and Articulation Control Subsystem (AACS) team, is responsible for guaranteeing that the pointing designs of each instrument execute safely and successfully onboard the spacecraft. The Cassini AACS estimates and controls the attitude of the three-axis stabilized Cassini spacecraft as it responds to ground-commanded pointing goals for the spacecraft's science instruments. To achieve the commanded targets within the required accuracy, AACS uses either RCS or RWA to control the spacecraft. Attitude determination sensors used by Cassini AACS include two stellar reference units (star trackers), two sun sensor assemblies, and two inertial reference units [2].

II. Attitude Control of the Cassini Spacecraft

A. Spacecraft Configuration

A sophisticated interplanetary spacecraft, Cassini is one of the largest spacecraft humans have ever built and launched. The orbiter, shown in Fig. 1, is about 6.8 m in height with a "diameter" of 4 m. The total mass of the spacecraft at launch was approximately 5574 kg, which included about 3000 kg of bipropellant. Cassini is a flexible spacecraft containing four structural appendages and three propellant

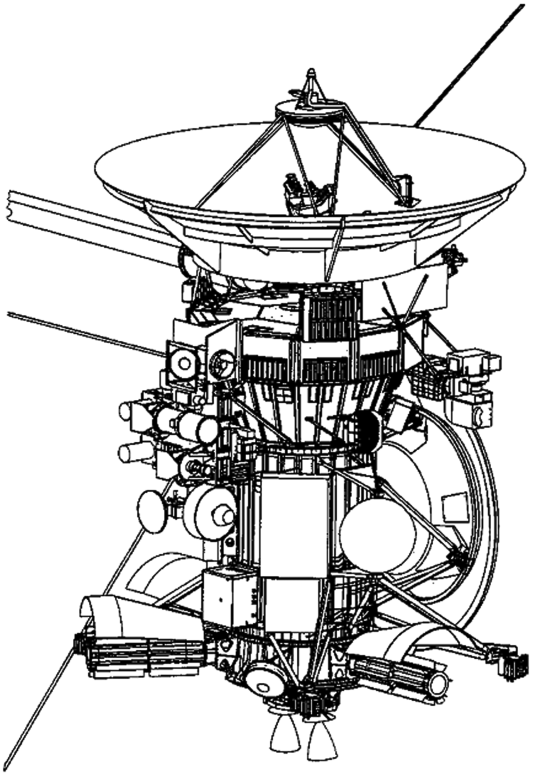

Fig. 1 Cassini spacecraft configuration.

tanks. The four appendages include the 11-m-long magnetometer boom and three similar radio and plasma wave science (RPWS) antennas. The fundamental frequency of the magnetometer boom is 0.67 Hz, and its damping ratio is 0.2–1%. The RPWS antennas have a fundamental frequency of 0.13 Hz and a damping ratio of 0.2%.

The propulsion module houses two cylindrical tanks with hemispherical end domes. These tanks each contain an eight-panel propellant management device (PMD) of the surface tension type. These PMDs are used to control the orientation of the propellant in the low-g environment via surface tension forces. When the spacecraft attitude is controlled by a set of three reaction wheels or eight thrusters, the bipropellant is in a so-called low-g sloshing mode. In this mode, the propellant will assume a shape determined by surface tension forces and the geometry of the PMD. At the end of the prime mission, the fill fractions of these tanks are about 20%. The corresponding fuel sloshing frequencies are estimated to be 3–5 mHz [3]. The damping ratio of the fuel sloshing motion in the low-g mode is estimated to be 10% [3].

B. Attitude Control by Either Reaction Wheels or RCS Thrusters

A high level of spacecraft-pointing stability is needed during imaging operations of optical remote sensing instruments such as the narrow angle camera (NAC). Typically, the required level of pointing stability is not achievable with an orbiter controlled by thrusters. Instead, three RWAs are employed for this purpose. At times imaging science is collected in RCS control due to engineering requirements. For example, immediately following the Saturn orbit insertion activity the spacecraft remained in RCS control for engineering purposes, but scientists took advantage of the proximity of Saturn and its rings to collect unique science. Similarly, during low-altitude flybys of Saturn's moons, for safety concerns the spacecraft is controlled by the RCS thrusters while the science teams continuously collect data. The controller designs of both the reaction wheels and thrusters are briefly reviewed in the following paragraphs.

The design of the RWA-control system for the Cassini spacecraft is described in [4]. As a requirement, the reaction-wheel attitude-control (RWAC) system must control the spacecraft with per-axis attitude-control errors that are within ± 40 μrad. While under reaction-wheel control, the spacecraft-pointing stability must be better than the requirements specified for a range of exposure times listed in Table 1. The spacecraft's principal axes are closely aligned with the spacecraft's mechanical axes, allowing the basic architecture of the RWAC to be a decoupled, three-axis, proportional and derivative (PD) controller. Because of the presence of bearing drag torque in the reaction wheels, a PD controller cannot drive the spacecraft attitude-control error to zero unless an integral term is added to the PD controller. This difficulty was overcome by adding a proportional and integral estimator of the RWA bearing drag torque in the flight software. The RWAC design has a bandwidth of 0.0299 Hz that allows the RWAC to arrest low-g fuel sloshing vibratory motions without exciting structural modes [4].

Table 1 Cassini pointing control, knowledge, and stability requirements

Pointing requirements	Requirements	Remarks
Science inertial pointing requirements (radial 99%)	(mrad)	Applicable only when spacecraft is quiescent
Control	2.0	
Knowledge	1.0	
Science pointing-stability requirements (2-σ per axis) for time windows of [2,7,9]:	(μrad)	Applicable only when spacecraft is quiescent
0.5 s	4	ISS, VIMS
1 s	8	ISS, VIMS
5 s	36	CIRS
22 s	100	CIRS
100 s	160	ISS, VIMS, CIRS
900 s	200	VIMS
1200 s	220	ISS
1 h	280	UVIS

In flight, the RWAC was first used on 16 March 2000, several months before the start of the Jupiter campaign. At the start of the prime mission (30 June 2004), the following per-axis slew rate and acceleration limits were used to slew the spacecraft using the reaction wheels: [1.65, 1.78, 3.08] mrad/s and [9, 10, 17] μrad/s^2 about the spacecraft's X, Y, and Z axes, respectively. These slew-profile limits were selected to be consistent with the capabilities of the reaction-wheel torque and the momentum-storage capacity without exceeding the 90 W of power allocated for the three reaction wheels.

A conventional bang-off-bang (BOB) thruster control algorithm is used by the Cassini AACS [5]. The BOB algorithm uses error signals that are the weighted sums of per-axis attitude errors and attitude rate errors to control thruster firings. The spacecraft's attitude-control errors while on thruster control are "commandable" via a command setting the allowable per-axis dead banding. The three arguments of this command provide the flight software with the desired magnitudes of the controller dead band about the spacecraft's axes. During the early cruise phase of the mission with the high-gain antenna pointed at Earth for X-band communication, a dead band of [2, 2, 20] mrad along the body-fixed XYZ frame was used to assure that the inertial pointing-control requirement for the X-band downlink was achieved. At times when accurate pointing was not needed, AACS used a dead band of [20, 20, 20] mrad along the body-fixed XYZ frame to save both hydrazine and thruster on/off cycles. On the other hand, on several occasions the attitude-control dead band along the body-fixed XYZ frame was tightened to [2, 2, 2] mrad or even [0.5, 0.5, 0.5] mrad to satisfy the science teams' pointing requirements. The bandwidth of the RCS attitude controller is selected to be 0.15 Hz, which is significantly higher than the low-g bipropellant sloshing frequencies. The minimum impulse bit of these thrusters is on the order of 7–8 ms.

From the spacecraft's launch in 1997 through 2003, Cassini predominately used a set of eight thrusters to control the spacecraft's attitude. During the tour (within the Saturn system), the spacecraft is slewed mainly using three prime reaction wheels. Thrusters are primarily used to control the spacecraft's attitude during low-altitude Titan flybys (to overcome the aerodynamic torque of Titan's atmosphere), biasing the reaction wheels' angular momentum vectors, and to perform small trajectory correction maneuvers.

III. Pointing Control and Stability Requirements

Spacecraft-pointing control error is defined as the angle between the actual pointing direction and the desired pointing direction of a particular onboard body vector. The spacecraft's pointing-control requirements are driven by the need to guarantee that the selected science target falls inside the field of view of the science instrument (see Table 1 for details of Cassini's pointing-control requirements). If the 2 mrad (radial 99%) pointing-control requirement for NAC is met, the captured image is guaranteed to fall inside the 6.1×6.1 mrad field of view of the NAC.

Spacecraft-pointing stability is defined as the angle variation of the actual pointing direction of an onboard body vector over a time duration called the "exposure time" (or "dwell time"). The spacecraft's pointing-stability requirements are driven by the need to ascertain that, over the exposure time of the imaging, incoming photons are "focused" on the intended set of camera charge-coupled device pixels. If the instrument moves during the exposure time, photons fall on the intended set of pixels as well as neighboring pixels, resulting in a fuzzy image. The science-driven pointing-stability requirements selected correspond to a tolerable degradation of image quality.

A. Science-Driven Pointing Requirements

Cassini carries 12 scientific instruments, half of which are considered remote sensing instruments based on the objects that they observe. The six remote sensing instruments are the imaging science subsystem (ISS), the visible and infrared mapping spectrometer (VIMS), the composite infrared spectrometer (CIRS), the ultraviolet imaging spectrograph (UVIS), the Cassini radar, and the radio science subsystem.

The first four of these instruments are mounted and coaligned on the remote sensing pallet. The ISS consists of two cameras, the narrow angle camera and the wide angle camera (WAC). The field of view of the NAC is 6.1×6.1 mrad (± 3.05 mrad), whereas the WAC field of view is 61.2×61.2 mrad. The NAC boresight vector is nominally aligned with the $-Y$ axis of the spacecraft. With a field of view of only a few milliradians, the pointing of these remote sensing instruments must be made with great care. Tables 2 and 3 summarize the flight performance of the spacecraft-pointing control and pointing knowledge, respectively. Both the inertial pointing control and pointing knowledge requirements (listed in Table 1) are met with margins.

B. Sources of Spacecraft-Pointing Jitter

Spacecraft jitter control is effective only when the causes of jitter are well understood. Jitter experienced by a spacecraft can be attributed to the performance of the onboard sensors and actuators, disturbances introduced during nominal operations, and the spacecraft's interaction with the external environment. The following sources of jitter are applicable to Cassini operations.

Sources of jitter inherent to the spacecraft include the reaction wheels' imperfections, low-g fuel sloshing motion, and sensor noise. The static imbalance of an RWA generates a rotating force that is proportional to the squared spin rate of the wheel. This force, in turn, generates a torque about the spacecraft's center of mass. The RWA dynamic imbalance generates a rotating torque that is proportional to the squared spin rate of the wheel. Other RWA-related disturbance sources include bearing drag torque, the finite size of the least significant bit of the digital-to-analog torque commands, and others. The dynamics of low-g fuel sloshing motion was described in Sec. II. At tank fill fractions of 20, 50, and 70%, the fuel sloshing frequencies are estimated to be 3–5, 2–4, and 4–6 mHz, respectively [3]. However, the uncertainties associated with these frequency estimates are large. Sensor noise with a significant frequency content within the controller bandwidth looks like valid "commands" to the attitude controller. Accordingly, the controller generates control torque to cause the spacecraft attitude to follow these erroneous commands. This results in undesired spacecraft motion.

Jitter can be induced during nominal spacecraft operations, such as structural vibration caused by slewing and disturbances resulting from payload articulation mechanisms. When a spacecraft is slewed from one inertial attitude to another, residual structural vibration after the completion of the slew might be significant. The magnitude of these residual vibrations is related to both the natural frequencies and damping ratios of the dominant spacecraft structural and sloshing modes. They are also related to the magnitude of the angular acceleration used while slewing the spacecraft, as well as the elapsed time between the end of the slew and the time at which the science observations begin. Further information about the magnitude of the residual vibratory spacecraft attitude after a slew is provided in [7].

Table 2 Cassini pointing-control performance

Error sources	3-σ per axis, mrad		Remarks
	X axis	Z axis	
Attitude estimation error	0.027	0.01	Flight performance[a]
Star tracker geometric distortion errors	0.3	0.03	Flight calibration results[a]
Calibration error of NAC bore-sight vector	0.014	0.0023	Flight calibration results[a]
Thermal mechanical instability of the star tracker bore-sight vector	0.2	0.2	Ground test results
Thermal mechanical instability of the NAC bore-sight vector	0.07	0.41	Flight performance[a]
Reaction-wheel attitude controller error	0.04	0.04	Flight performance[a]
Error of the science target vector (as modeled by a pointing vector in flight software)	0.04	0.04	Ground software capability
Mispointing due to timing error	0.037	0.037	Flight hardware limitation
Command resolution error of the science target vector	0.048	0.048	Flight software implementation error
Error in representing the NAC bore-sight vector as a fixed body vector in flight software	0.048	0.048	Flight software implementation error
Per-axis capability	0.416	0.618	Individual error sources are uncorrelated except for the thermal/mechanical instability of the tracker and NAC (which is fully correlated)
Radial 99% capability $\approx 2.575 \times \text{rss}(\sigma_X, \sigma_Z)$	0.639		If per-axis errors are fully correlated (worst case)
Radial 99% capability $\approx 2.146 \times \text{rss}(\sigma_X, \sigma_Z)$	0.533		If per-axis errors are not correlated (best case)
Radial 99% requirement[b]	2.00		*Requirement is met*

[a]Reference [2] provides details on how the star tracker is calibrated in flight as well as the results of calibrations. Flight calibration performance of the NAC bore-sight vector is also given in that reference.

[b]The spacecraft-pointing control requirement is expressed in terms of a "radial 99%" statistic. This statistic is used because of the need to control the deviation of the bore-sight vector of the imaging instrument (along the spacecraft's Y axis) from the target vector. Let e_X and e_Z denote the per-axis pointing-control errors about the spacecraft's X and Z axes, respectively. A 2 mrad radial 99% pointing-control requirement is one that drives the system design to have 99% of the total pointing-control error data, $e_T = (e_X^2 + e_Z^2)^{1/2}$, to be <2 mrad.

Table 3 Cassini pointing knowledge performance

Error sources	3-σ per axis, mrad: X axis	Z axis	Remarks
Attitude estimation error	0.027	0.01	Flight performance[a]
Star tracker geometric distortion errors	0.3	0.03	Flight calibration results[a]
Calibration error of NAC bore-sight vector	0.014	0.0023	Flight calibration results[a]
Thermal mechanical instability of the star tracker bore-sight vector	0.2	0.2	Ground test results
Thermal mechanical instability of the NAC bore-sight vector	0.07	0.41	Flight performance[a]
Telemetry quantization error	0.005	0.005	Flight software implementation error
Error due to timing error	0.002	0.002	Timing error is 10 ms
Per-axis capability	0.405	0.611	Individual error sources are uncorrelated except for the thermal/mechanical instability of the tracker and NAC (which is fully correlated)
Radial 99% capability $\approx 2.575 \times \text{rss}(\sigma_X, \sigma_Z)$	0.629		If per-axis errors are fully correlated (worst case)
Radial 99% capability $\approx 2.146 \times \text{rss}(\sigma_X, \sigma_Z)$	0.524		If per-axis errors are not correlated (best case)
Radial 99% requirement[b]	1.00		*Requirement is met*

[a]Reference [2] provides details on how the star tracker is calibrated in flight as well as the results of calibrations. Flight calibration performance of the NAC bore-sight vector is also given in that reference.
[b]For a definition of the radial 99% statistic, see the footnote of Table 2.

An articulation mechanism of the cosmic dust analyzer science instrument permits the instrument to be rotated to several positions relative to the orbiter. These articulation motions impart disturbance torque on the base body of the spacecraft. Additionally, the NAC has 24 filter wheels that can impart disturbance torque on the base body when changed.

The spacecraft can also experience jitter caused by environmental disturbance torques and thermal gradients. During a low-altitude flyby of Titan, the spacecraft experiences significant aerodynamic torque due to the Titan atmosphere. Similarly, during a low-altitude flyby of Enceladus, the spacecraft experiences disturbance torque due to the watery plume clouds. This torque must be countered by frequent thruster firings, and the corresponding spacecraft motion is very jittery. Other environmental torques include a solar-radiation torque, a radiation torque from three power generators, and a gravity-gradient torque. Thermal gradient caused by reorientation of the spacecraft base body will cause thermal/mechanical snaps, creep strain relief "popping" (structural annealing), and microstick slip at loaded mechanical joints.

IV. Spacecraft-Pointing Stability

The following section discusses two methods to quantify pointing stability, the "peak-to-peak" and the "rms" method for calculating pointing stability. Both methods are applied to a set of test data from the Cassini prime mission. The relative characteristics of these two pointing-stability metrics are compared using the results.

A so-called peak-to-peak pointing-stability metric is commonly used to specify the level of motion stability of the line-of-sight (LOS) vector of an onboard instrument. This method was used, for example, on both Voyager missions and on the Mars Pathfinder mission. Mathematically, the peak-to-peak stability metric is given by

$$s_P(t,T) = \max_{\tau\in[0,T]} |\phi(t+\tau) - \phi(t)| \tag{1}$$

$$\sigma_{SP}^2(T) = E\{s_P^2(t,T)\} = \frac{1}{N}\sum_{t_i=t_1}^{t_i=t_N} s_P^2(t_i,T) \tag{2}$$

One obvious drawback of this pointing-stability metric is that it uses only the two extrema points in the time history of the pointing error that fall within a time window of interest T. Another weakness of this pointing-stability metric is that the degree to which disturbances at different frequencies contribute to jitters is not captured or easily extracted using this metric. For this reason, Cassini AACS designers adopted a new metric, termed the root-mean-square pointing stability that compares pointing-stability deviations with the mean within a defined window of interest. Graphical illustrations of both methods are depicted in Fig. 2.

The rms pointing-stability metric, σ_{rms}, was first introduced by Lucke et al. [6], and it has since been adopted by both the Cassini Mission and the Space Interferometry Mission [7]. Mathematically, the rms stability metric is defined as follows:

$$m(t,T) = \frac{1}{T}\int_t^{t+T} \phi(\tau)\,\mathrm{d}\tau \tag{3}$$

$$e(\tau,t,T) = \phi(\tau) - m(t,T) \tag{4}$$

$$\sigma_W^2(t,T) = \frac{1}{T}\int_t^{t+T} e^2(\tau,t,T)\,\mathrm{d}\tau \tag{5}$$

$$\sigma_{\text{rms}}^2(T) = E\{\sigma_W^2(t,T)\} = \frac{1}{N}\sum_{t_i=t_1}^{t_i=t_N} \sigma_W^2(t_i,T) \tag{6}$$

Applying Eqs. (3–5) on the first set of $\phi(\tau)$ data, $t_1 < \tau < t_1 + T$, one obtains $\sigma_W^2(t_1,T)$. Repeating the process N times, one obtains $\sigma_W^2(t_N,T)$. As indicated in Eq. (6), $\sigma_{\text{rms}}^2(T)$ represents the mean value of $\sigma_W^2(t_i,T)$ $(i = 1,\ldots,N)$.

In the frequency domain, the rms stability metric [6] is given by

$$\sigma_{\text{rms}}^2(T) = \int_0^\infty \Phi_{\text{PSD}}(f) W(f,T)\,\mathrm{d}f \tag{7}$$

Here, $\Phi_{\text{PSD}}(f)$ is the power spectral density (PSD) of $\phi(t)$ in rad^2/Hz. The frequency weighting function is given by

$$W(f,T) = W(C) = 1 - \frac{2(1-\cos C)}{C^2} \tag{8}$$

where

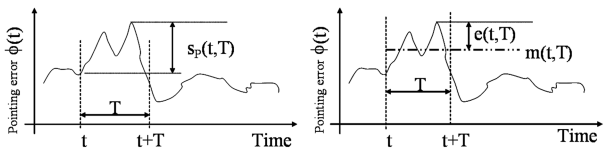

Fig. 2 Representative calculation: a) peak-to-peak pointing stability, and b) rms pointing stability.

Table 4 Peak and rms pointing-stability metrics, μrad

	Peak-to-peak stability	RMS stability (2-σ per axis)	
Spacecraft axes	Time domain	Time domain	Frequency domain
		100 s exposure time	
X axis	6.1	3.8	3.8
Z axis	8.0	5.0	4.9
		1200 s exposure time	
X axis	8.0	4.0	3.8
Z axis	11.3	5.7	5.5

$$C = 2\pi f T \tag{9}$$

As explained in [6,7], $W(C)$ functions as a high-pass filter. Only vibratory motions whose frequencies are high relative to the exposure time T are contributing to the rms stability metric.

As an illustration, both the peak and the rms pointing-stability metrics were applied to an RWA-based WAC observation (from 2007-DOY164 at 14:46 through 2007-DOY164 at 15:45, where the time convention used is defined as year, followed by day of year (DOY) at a given hour, then minute). Table 4 compares the results using the RWA data describing the three per-axis attitude-control errors estimated by the flight software. The spacecraft was quiescent with all three per-axis attitude rates lower than 0.01 deg/s throughout this observation period. The approximate moments of inertia of the spacecraft at the time of this observation were [7110, 5900, 3670] kg $\cdot$ m^2 about the X, Y, and Z axes, respectively. Figure 3a depicts the time history of the X-axis attitude error telemetry. These telemetry data were recorded at 2 s intervals. To eliminate slew-induced transients, telemetry was processed only after 200 s from the last rest-to-rest slew, and the WAC observation started at 2007-DOY164 at 14:46. Figure 3b depicts the weighted PSD of the X-axis time data, for a 100 s exposure time, in log–log scale. Finally, Fig. 3c shows the cumulative pointing stability versus frequency for a 100 s exposure window. Table 4 compares the pointing-stability metrics for two exposure times (100 and 1200 s) for the X and Z axes. These data were selected because the boresight axis of the WAC is nominally aligned with the spacecraft's minus Y axis; therefore only pointing-stability metrics about the X and Z axes are of interest.

From results given in Table 4, as expected we observe that the peak-to-peak stability metric is always larger than its rms stability metric counterpart. Results given in Fig. 3 and in Table 4 both suggest that the peak-to-peak values are 1.2–2.3 times larger than their (2-σ) rms pointing-stability counterparts. The pointing stability about the Z axis is always larger than its X-axis pointing-stability counterpart. This is because the spacecraft Z-axis moment of inertia is smaller than the X-axis moment of inertia. The achieved rms stability for exposure times of 100 and 1200 s are both at least an order of magnitude better than their respective requirements (see Table 1). The rms pointing-stability metrics computed using the time-domain approach [Eq. (6)] closely approximate those computed using the frequency-domain approach [Eq. (7)]. Moreover, time-domain results always bound their frequency-domain counterparts. The cumulative pointing stability depicted in Fig. 3c shows a "sudden" improvement in stability at frequencies near 0.03–0.034 Hz. This is due to control action on the part of the RWA controller (whose bandwidth is 0.03 Hz). Further analysis of Cassini telemetry in Sec. V uses the rms method to characterize the performance of the Cassini pointing stability in both RWA- and RCS-control modes.

V. Spacecraft-Pointing-Stability Performance

The following section presents the pointing-stability results from 2003 through 2008 while the spacecraft collected science in either the RCS or RWA-control mode. The per-axis attitude-control errors were used for the pointing-stability calculations at 2 s intervals. The error expected from processing the 32-bit floating-point telemetry channel is bounded by ± 0.1 μrad. With data collection at 2 s intervals, our analysis of the pointing stability was limited to a frequency range of 0–250 mHz (Nyquist foldover frequency of 0.5 Hz sampled data).

A. Flight Performance of Cassini RWA Pointing Stability

Ten sets of data were collected and analyzed to generate a range of Cassini's pointing-stability performance from 2003 through 2008. Doppler tracking experiments (also called the gravitational-wave experiment, GWE) using the Earth and the spacecraft as test masses were conducted by Cassini for gravitational-wave searches in the low frequency range (10^{-4}–10^{-3} Hz). For time periods ranging between 20 and 40 days centered about its solar opposition, the spacecraft was tracked continuously (in Ka band) in the search for gravitational waves that were predicted by Einstein's general relativity theory [8]. The third and final search was 19 days long, conducted from 12–30 November 2003. The pointing-stability results from this search are included as a case study of Cassini's RWA pointing-stability performance. Along with data collected from GWE-3, nine other "point and stare" science observations were selected for analysis to represent a complete picture of the Cassini pointing performance during the prime mission. The results of all 10 cases are summarized in Table 5. The dependency of the spacecraft-pointing stability on exposure time, in log–log scale, is depicted in Fig. 4. Superimposed on these plots is the pointing-stability requirement curve based on data from Table 1. These data points overwhelmingly confirm that the Cassini pointing-stability performance while in RWA control meets the requirements specified in Table 1 with significant margin. The quality of images returned by the high-resolution cameras provides ample evidence to this claim (see also Fig. 9).

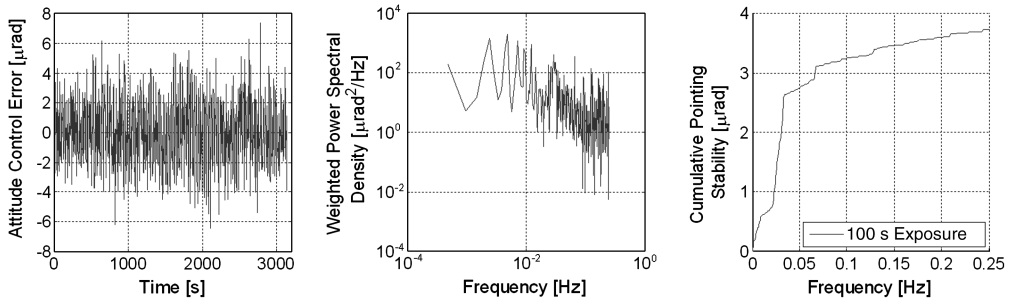

Fig. 3 Shown are the following: a) time history of X-axis attitude control error, b) the weighted PSD result, and c) the cumulative pointing stability.

Table 5 RMS pointing-stability performance in RWA control, 2-σ per axis, μrad

Year-day of year	Exposure time, s			
	5	22	100	1200
	X axis			
2003-DOY328	2.1	2.7	3.0	3.0
2004-DOY136	2.1	2.9	3.0	3.0
2004-DOY261	2.3	3.1	3.4	3.6
2005-DOY102	2.3	3.0	3.6	3.7
2006-DOY086	2.1	2.8	3.0	3.3
2006-DOY307	2.2	2.8	3.1	3.2
2007-DOY126	2.4	3.3	3.6	3.8
2007-DOY355	2.2	2.8	3.2	3.4
2008-DOY007	2.3	3.0	3.5	4.0
2008-DOY113	2.3	3.0	3.6	3.9
	Y axis			
2003-DOY328	1.9	2.6	2.9	3.0
2004-DOY136	2.1	3.5	3.6	3.7
2004-DOY261	2.1	2.6	2.8	2.8
2005-DOY102	2.2	2.8	3.3	3.3
2006-DOY086	2.0	2.5	2.7	2.8
2006-DOY307	2.1	2.7	2.8	2.9
2007-DOY126	2.3	3.2	3.5	3.6
2007-DOY355	2.3	3.0	3.1	3.2
2008-DOY007	2.2	2.7	3.0	3.0
2008-DOY113	2.1	2.7	2.8	2.8
	Z axis			
2003-DOY328	2.1	3.0	3.4	3.5
2004-DOY136	2.3	3.2	3.9	4.3
2004-DOY261	2.4	3.2	3.4	3.5
2005-DOY102	2.2	3.0	3.3	3.3
2006-DOY086	2.2	3.6	5.1	5.4
2006-DOY307	2.4	3.6	4.6	4.9
2007-DOY126	2.4	3.8	5.0	5.3
2007-DOY355	2.3	3.6	5.0	5.2
2008-DOY007	2.3	3.7	5.2	5.5
2008-DOY113	2.3	3.7	5.1	5.3

For each of the 10 cases, the cumulative pointing stability versus frequency was analyzed to determine the sources of pointing jitters. Figure 5 presents charts of the results for each axis over various exposure times (5, 22, 100, and 1200 s) for the GWE-3 that began on 12 November 2003. From these charts, one can make several interesting observations. Without loss of generality, let us focus our attention on the frequency dependency of the *X*-axis cumulative pointing stability given in Fig. 5a. The four curves plotted in this figure, from the top, are those for exposure times of 1200, 100, 22, and 5 s. Within the frequency range of 0–0.05 Hz, we notice that the cumulative pointing stability of the top three curves (with exposure times of 1200, 100, and 22 s) increases sharply with frequency but

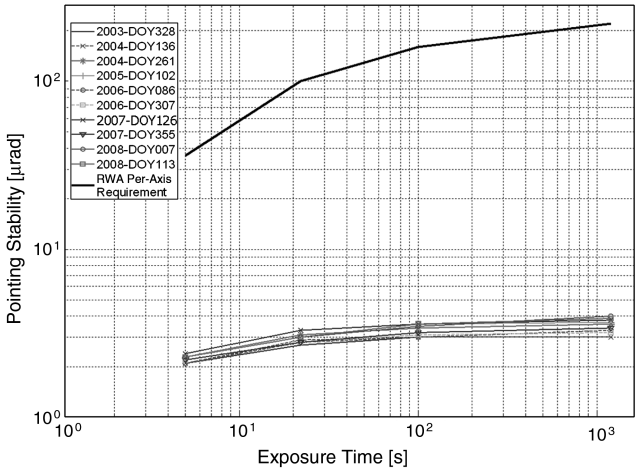

Fig. 4 Summary of *X*-axis pointing-stability performance (rms method, 2-σ) while in RWA control.

this observation is not true for the fourth curve (corresponding to an exposure time of 5 s). In fact, for the top three curves, at least 50% of the steady-state values of the cumulative pointing-stability levels are contributed by disturbance sources with frequencies that fall within 0–0.05 Hz. One example of these disturbance sources is the low-*g* fuel sloshing motion discussed in Sec. III.B. To understand why the "slope" of the fourth curve (for a 5 s exposure time) is small when compared with those of the other three curves, let us compute the crossover frequency for a 5 s exposure time. Only vibratory motions whose frequencies are higher than the crossover frequency will make a significant contribution to pointing jitter. With reference to Eqs. (8) and (9) given in Sec. IV, we note that $W(C) \geq 0.5$ when $C \geq 2.78$. Therefore, the crossover frequency for a 5 s exposure time is $2.78/(2\pi \times 5) \approx 0.088$ Hz. The estimated values of low-*g* fuel sloshing motions are lower than this crossover frequency; thus, although low-*g* fuel sloshing motions contributed significantly to pointing jitter for imaging with long exposure time, its contribution to pointing jitter of imaging with short exposure time is limited.

Another interesting observation one can make from the curves depicted in Fig. 5a is the "step" increase in the pointing jitter near a frequency of 0.13 Hz. This could be due to the vibratory motions of the three RPWS antennas (whose fundamental frequency is estimated at 0.13 Hz and has a 0.2% damping ratio). If the contribution of the RPWS vibratory motions to pointing jitter is unacceptably large (this is not the case according to Fig. 5), one might want to consider, for example, the addition of passive damping to the RPWS system. The identification of jitter sources via the cumulative pointing-stability plots is a key advantage of using the rms stability metric.

From Fig. 5, one notes that the *Z*-axis pointing-stability performance (as depicted in Fig. 5c) is worse than the pointing-stability performance about the other two axes. Also, the *X*-axis pointing-stability performance is (slightly) worse than that of the *Y* axis. This trend is present in each of the data sets analyzed and is not limited to data depicted in Fig. 5. These trends could be explained as follows. The *Z*-axis pointing-stability performance is worse than its *X*-axis and *Y*-axis counterparts because of the spacecraft's smaller *Z*-axis moment of inertia. The *X*-axis pointing-stability performance is worse than its *Y*-axis counterpart due to the reduced *X*-axis attitude determination performance (see also Tables 2 and 3). The boresight vector of the star tracker is parallel to the spacecraft's *X* axis and as a result, the attitude estimation error about the *X* axis is worse than those achieved about the *Y* and *Z* axes. The pointing-stability performance about the *X* axis suffers due to this increased attitude estimation error about the corresponding axis.

B. Spacecraft-Pointing Stability Performance in RCS-Controlled Mode

The RCS-based pointing-stability performance of Cassini for five selected science observations (on 2004-DOY181, 2004-DOY360, 2007-DOY115, 2007-DOY200, and 2008-DOY004) is summarized in Table 6. Figure 6 depicts the dependency of the spacecraft-pointing stability on exposure time, in log–log scale. Superimposed on these plots is the curve of the RWA-based pointing-stability requirements (see Table 1). Note that for exposure times of less than 40 s, all RCS-based *X*-axis pointing-stability performance meets the RWA-based pointing-stability requirements. Pointing-stability requirements for exposure times $\geq$ 100 s are harder to achieve with RCS thrusters. Reaction wheels must be employed to meet these requirements. The nearly linear relation between the change in pointing stability, in log scale, and exposure time, also in log scale, suggests the following approximate relation:

$$\Delta\theta = KT^{\beta} \tag{10}$$

Estimated values of the coefficients K and β are given in Table 6.

Time histories of the per-axis attitude-control errors for the five RCS-based science observations are documented in [9]. To investigate the effect of commanded dead band on the RCS pointing-stability performance, three time histories of *Z*-axis attitude-control errors are depicted in Fig. 7, corresponding to three distinct dead-band settings of 0.5, 2, and 20 mrad. As indicated in Fig. 7, these

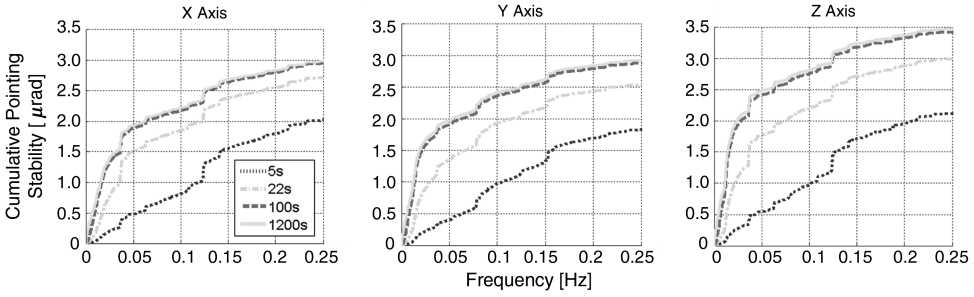

Fig. 5 Cumulative pointing stability (2-σ) in RWA control for various exposure windows.

three sets of telemetry data correspond to three different mission phases (in 2004, 2007, and 2008) with significant differences in inertial properties. Figure 8 compares the pointing-stability results for these three cases. From results given in Table 6 and Figs. 7 and 8, we observe that RCS-based pointing-stability performance is strongly related to the commanded dead band. Pointing stability will degrade with the use of a "large" dead band. This result is shown in Fig. 8 for a short exposure time of 5 s, where the Z-axis pointing stability of the 2008-DOY004 observations (with a dead band of 2 mrad) is better than that of 2004-DOY360 observations (with a dead band of 20 mrad). This is the case in spite of the fact that the Z-axis moment of inertia of the spacecraft in 2004-DOY360 was larger than its counterpart in 2008-DOY004 due to fuel consumption. One can draw a similar conclusion using pointing-stability performance determined for a larger exposure time of 1200 s (see Fig. 8). A large attitude controller dead band permits the spacecraft to traverse a large angular displacement before the motions is arrested by RCS thruster firings. As a result, different parts of the intended target are captured during a long exposure and a smeared image is produced. On the other hand, a very small attitude controller dead band promotes frequent "reversals" of the spacecraft's attitude that also degrade the pointing-stability performance (for small exposure times). There exists a dead-band setting that optimizes the pointing-stability performance, but that "optimal" dead band could only be determined via flight experience. For example, for a 5 s exposure time, the pointing-stability performance obtained with a 2 mrad dead band is better than that obtained with a 0.5 mrad dead band (the inertial properties of the spacecraft at the times of these data sets are quite comparable).

Repeatability of RCS pointing-stability performance is poor (relative to RWA's). Compare, for example, the pointing-stability

Table 6 RMS pointing-stability performance in RCS control, 2-σ per axis, μrad

Year-day of year	Dead band, mrad	Exposure time T, s				Fit parameters: $\Delta\theta \approx KT^{\beta}$	
		5	22	100	1200	K	β
		X axis					
2004-DOY181	2.0	8	27	119	1206	1.70	0.92
2004-DOY360	2.0	14	55	238	1393	3.52	0.89
2007-DOY115	2.0	9	30	128	1269	1.72	0.96
2007-DOY200	0.5	19	74	224	862	7.66	0.69
2008-DOY004	2.0	11	42	183	1607	2.24	0.96
		Y axis					
2004-DOY181	2.0	7	25	107	991	1.59	0.91
2004-DOY360	2.0	15	60	257	1388	3.95	0.87
2007-DOY115	2.0	9	31	135	1421	1.66	0.98
2007-DOY200	0.5	19	77	209	622	9.11	0.62
2008-DOY004	2.0	11	42	182	1623	2.23	0.96
		Z axis					
2004-DOY181	20.0	14	33	101	1079	3.17	0.80
2004-DOY360	20.0	29	65	211	2288	5.71	0.85
2007-DOY115	20.0	53	150	612	6748	9.61	0.94
2007-DOY200	0.5	26	100	325	693	13.5	0.60
2008-DOY004	2.0	13	53	224	1423	3.18	0.91

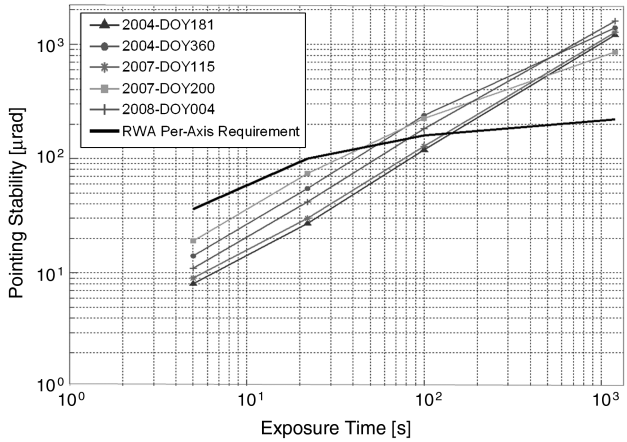

Fig. 6 Summary of X-axis pointing stability (rms method, 2-σ) while in RCS control.

performance (about all three axes) of two science observations (both with a 2 mrad dead band): 2004-DOY181 and 2004-DOY360. Pointing-stability performance of the 2004-DOY360 data is approximately a factor of 2 worse than the corresponding pointing-stability performance from the 2004-DOY181 data. Attitude-control limit cycle is a function of many factors, including disturbance torque, moment of inertia, reproducibility of the thruster's force, and others. At best, one can only put gross bounds on the RCS-based pointing-stability performance.

The limit cycle behavior of the Z-axis attitude-control error near 2007-DOY200 at 22:55 (Fig. 7a) could be explained as follows. The Z-axis rates of the spacecraft before and after reaching the negative edge of the dead band are Ω_{before} (-7.62 μrad/s) and Ω_{after} ($+5.33$ μrad/s). Accordingly, the size of the two thrusters' pulses fired is

$$\Delta T_{\text{pulse}} \approx \frac{I_{ZZ}(\Omega_{\text{after}} - \Omega_{\text{before}})}{2LF} \tag{11}$$

Here, the Z-axis moment of inertia of the spacecraft is 3670 kg $\cdot$ m^2, the magnitude of each thruster force is approximately 0.85 N, and the moment arm of the thrusters is approximately 1.61 m. The size of this particular pair of pulses, 17.4 ms, is larger than the minimum impulse bit of the Cassini thrusters (7–8 ms). Properly tuned, the Cassini RCS attitude controller has the potential to improve the spacecraft-pointing stability performance [9].

The time history of the Z-axis pointing-control error of the 2008-DOY004 science observations (see Fig. 7b) has a distinct behavior. It appears that thrusters' firings have excited a particular spacecraft flexible mode with a frequency of about 2.5 mHz (16 cycles in 1.8 h). These observed oscillations could be a low-g sloshing motion of the bipropellants in their tanks. As of 2008, the fill fractions of the tanks are approximately 13%. The corresponding fuel sloshing frequency was analytically predicted to be 3–5 mHz [3]. Similar oscillations, with frequency of 2.5–2.6 mHz, were also observed in the 2001

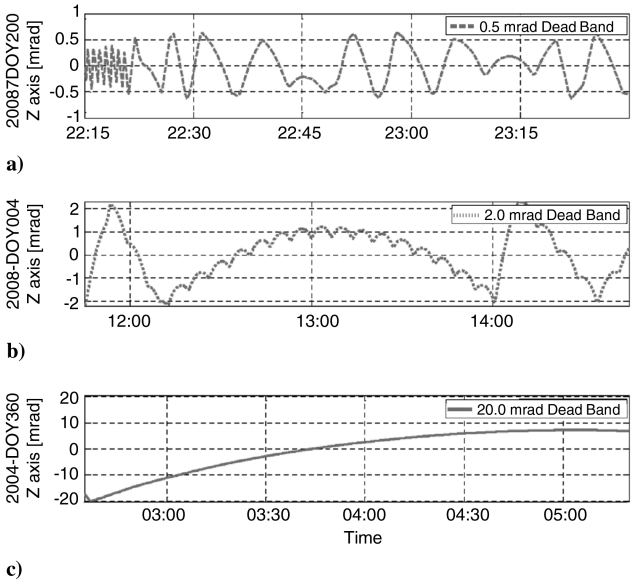

Fig. 7 *Z*-axis attitude-control errors for dead bands of 0.5, 2, and 20 mrad.

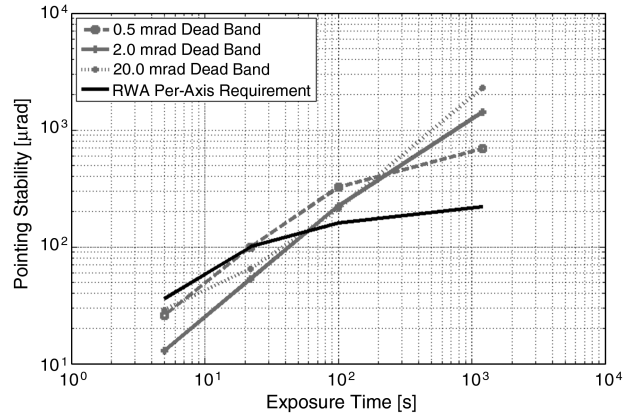

Fig. 8 RCS-controlled spacecraft-pointing stability for various dead bands.

(when the tank fill fractions were higher, at 80%) telemetry on the *Z*-axis attitude-control error [9]. Flight results seem to suggest that the low-g fuel sloshing frequency is 2.5–2.6 mHz regardless of the fill fractions of the tanks.

The Voyager spacecraft was controlled using 0.967 N thrusters. The pointing-stability requirement of the Voyager missions was set at 20 μrad/s while the "goal" was 10 μrad/s (that is, a pointing excursion of 50 μrad over 5 s). Nominal attitude controller dead band used was ± 0.88 mrad, and thruster pulse modes used were 10 and 60 ms. The 20 μrad/s pointing-stability requirement was achievable using the 10 ms pulse mode, but without using the RWAs, the 10 μrad/s goal was difficult to achieve for imaging science. However, in the later part of Voyager's extended mission, the operations team throttled back the thrusters' on time, ultimately reaching 4 ms during the last few planet encounters. The use of 4 ms thruster pulses contributed to the attainment of the 10 μrad/s pointing-stability requirement. Relative to this achievement, we note that the pointing-stability performance of Cassini in RCS control (see Table 6), in terms of the "instantaneous line-of-sight angular rate" (angular excursion of the LOS vector divided by the exposure time) is always better than 10 μrad/s.

VI. Conclusions

Cassini carries multiple high-resolution scientific instruments for which proper operations demand high spacecraft-pointing stability. Comprehensive analyses to assess Cassini in-flight pointing-stability performance over the past five years are performed in this work. Pointing-stability performance computed from 10 sets of RWA-controlled flight data indicates that all the requirements have been met with significant margin. Moreover, analyses of five sets of RCS-controlled flight data revealed that most of these pointing-stability requirements (that are only applicable when the spacecraft is controlled by the RWA) have even been met when the spacecraft was under thruster control.

Figure 9 shows three images taken by science instruments carried onboard the Cassini spacecraft. The foundation of these high quality images is the stability of the spacecraft basebody. Overall, the spacecraft is extraordinarily "quiet," which underlines the excellence of the overall attitude-control design (both software and hardware). The performances of RWA controller design, the star identification algorithm, as well as the attitude estimator are all impressive [2,4,10]. Results also confirmed that measures taken minimize internal excitations (such as the use of PMD to control liquid sloshing [3] and the very small static and dynamic imbalances of the reaction wheels [2,4], as well as the use of proper slew rate and acceleration limits [2]). Lessons learned from both the Cassini AACS design as well as in-flight operations practices should be studied by future missions if attaining high pointing-stability performance is critical to mission success.

Acknowledgments

The work described in this paper was carried out by the Jet Propulsion Laboratory, California Institute of Technology, under contract with NASA. David Bayard and Glenn Macala, our colleagues at the Jet Propulsion Laboratory, improved the technical accuracy of this paper with their careful reading. Also, we would like to thank the reviewers and the Associate Editor of the *Journal of Spacecraft and Rockets* for their comments on an earlier version of this paper.

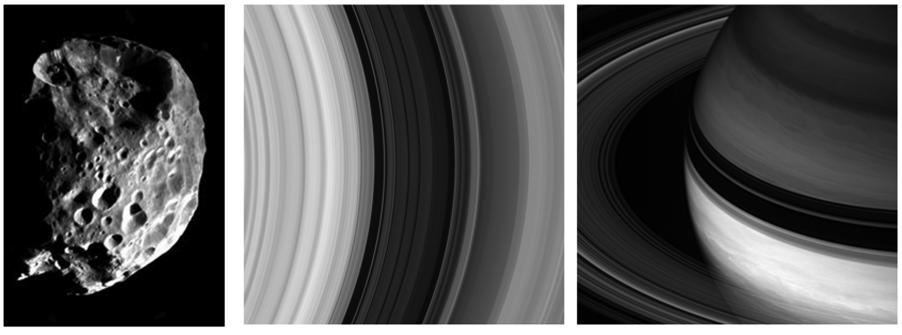

a) b) c)

Fig. 9 Shown are the following: a) RCS control: Phoebe; b) RWA control: rings; c) RWA control: Saturn and rings. (Credit: "In Orbit," Spacecraft Imaging Database, Cassini Imaging Central Laboratory for Operations, Boulder, CO.)

References

[1] Jaffe, L., and Herrell, L., "Cassini Huygens Science Instruments, Spacecraft, and Mission," *Journal of Spacecraft and Rockets*, Vol. 34, No. 4, 1997, pp. 509–521.
doi:10.2514/2.3241

[2] Lee, A. Y., and Hanover, G., "Cassini Spacecraft Attitude Control System Flight Performance," *Proceedings of the AIAA Guidance, Navigation, and Control Conference, and Exhibit*, AIAA, Reston, VA, 15–18 Aug. 2005.

[3] Enright, P., and Wong, E. C., "Propellant Sloshing Models for the Cassini Spacecraft," AIAA Paper 94-3730, 1994.

[4] Macala, G. A., "Design of the Reaction Wheel Attitude Control System for the Cassini Spacecraft," AAS Paper 02-121, 27–30 Jan. 2002.

[5] Chiang, R. Y., Breckenridge, W. G., and Wong, E., "Self-Tuning Thruster Control for Cassini Spacecraft," AIAA Paper 1996-3822, July 1996.

[6] Lucke, R. L., Sirlin, S. W., and San Martin, A. M., "New Definitions of Pointing Stability: AC and DC Effects," *Journal of the Astronautical Sciences*, Vol. 40, No. 4, Oct.–Dec. 1992, pp. 557–576.

[7] Lee, A. Y., Yu, J., Kahn, P., and Stoller, R., "Space Interferometry Mission Spacecraft Pointing Error Budgets," *IEEE Transactions on Aerospace and Electronic Systems*, Vol. 38, No. 2, April 2002, pp. 502–514.
doi:10.1109/TAES.2002.1008982

[8] Abbate, S. F., Armstrong, J. W., Asmar, S. W., Barbinis, E., Bertotti, B., Fleischman, D. U., Gatti, M. S., Glotz, G. L ., Herrera, R. G., Less, L., Lee, K. J., Ray, T. L., Tinto, M., Tortora, P., and Wahlquist, H. D., "The Cassini Gravitational Wave Experiment," *SPIE Proceeding*, Vol. 4856, SPIE–International Society for Optical Engineering, Bellingham, WA, 23–25 Aug. 2002.

[9] Burrough, E. L., and Lee, A. Y., "Pointing Stability Performance of the Cassini Spacecraft," *Proceedings of the 2008 AIAA Guidance, Navigation, and Control Conference*, AIAA, Reston, VA, 18–21 Aug. 2008.

[10] Alexander, J. W., and Chang, D. H., "Cassini Star Tracking and Identification Algorithms, Scene Simulation, and Testing," *SPIE Proceedings*, Vol. 2803, SPIE–International Society for Optical Engineering, Bellingham, WA, 1996, pp. 311–336.

C. Kluever
Associate Editor